MRI function in Bone Microstructure

Subjects: Biochemistry & Molecular Biology | Others | Engineering, Biomedical
Contributor: Enrico Soldati

Bone microarchitecture has been shown to provide useful information regarding the evaluation of skeleton quality with an added value to areal bone mineral density, which can be used for the di-agnosis of several bone diseases. Bone mineral density estimated from dual-energy x-ray absorp-tiometry (DXA) has shown to be a limited tool to identify patients' risk stratification and therapy delivery. Magnetic resonance imaging (MRI) has been proposed as another technique to assess bone quality and fracture risk by evaluating the bone structure and microarchitecture.

Keywords: MRI ; bone microarchitecture ; bone morphology ; bone quality

1. Introduction

1.1. Bone Disorders and Investigative Tools

A large number of studies have demonstrated the substantial burden of bone disorders worldwide [1][2][3]. Considered as the second greatest cause of disability [1], musculoskeletal pathologies account for 6.8% of total disability worldwide [2]. Bone pathologies are usually affecting the bones solid phase, which is composed of both cortical and cancellous/trabecular types of bone. Bone alterations commonly include cortical shell thinning, increased porosity of both cortical and trabecular bone phases [4][5], and reduced density, volume, and regenerative power. These bone modifications generally account for a reduced resistivity and flexibility eventually leading to an increased risk of fragility fractures accompanied by long-term disabilities. Recent studies have shown that people over the age of 50 with a high risk of osteoporotic fractures represented more than 150 million people worldwide with 137 million women [6]. This number is expected to exceed 300 million by 2040 [6]. Fragility fractures lead to more than half a million hospitalizations each year in North America alone, with an annual direct cost, which has been estimated to be $17 billion dollars in 2005. This cost is expected to rise by almost 50% by 2025 [7]. Overall, the early identification of bone fragility risk is a major health issue [8]. In the clinical context, bone disorders are usually assessed using dual-energy X-ray absorptiometry (DXA), which is able to assess the bone mineral density (BMD). The BMD score is then compared to a reference range of values calculated in healthy (25–35 years old) volunteers taking into account sex and ethnicity. Accordingly, a score (T-score) is generated indicating how far, in terms of SD (standard deviation), the measured BMD is from the reference values. A T-score between −1 and −2.5 indicates a low bone mass or osteopenia while a value lower than −2.5 is indicative of osteoporosis. The corresponding method has good sensitivity (around 88% for both men and post-menopausal women), but the specificity is poor (around 41% for post-menopausal women and 55% for men) [9] resulting in a low clinical diagnostic accuracy (70%) [10]. In addition, DXA measurements do not take into consideration microarchitectural alterations, which have also been recognized as part of the structural picture in osteoporosis. Of interest, bone microarchitecture can be assessed using quantitative computed tomography (qCT) [11][12]. Given that both DXA and qCT are both radiative imaging techniques, non-radiative alternatives would be of great interest. Over the last decades, magnetic resonance imaging (MRI) [13][14][15] has been indicated as a non-ionizing and non-invasive technique.

Using MRI, a large number of studies have attempted to assess bone microarchitecture in bone disorders and more particularly in osteoporosis [16][17][18][19]. The corresponding studies have been conducted at different magnetic field strengths, using different Radio Frequency coils and pulse sequences. Although, the results were compelling, the sensitivity of the corresponding microarchitecture metrics for diagnostic purposes and the assessment of the disease severity is still a matter of debate.

On the basis of a comparative survey of MRI, computed tomography, and DXA-based metrics, we intended to address the issues related to the diagnostic potential of the corresponding metrics and their capacity to predict disease severity. The final section will be devoted to potential perspectives offered by magnetic resonance spectroscopy (MRS) and chemical shift encoding (CSE-MRI), solid-state MRI, and quantitative susceptibility mapping (QSM).

1.2. Bone Microstructure

Bone is a multiphase material composed of a solid phase and a viscoelastic component. The solid phase is considered as hierarchical, anisotropic, and heterogeneous and is composed of 65% of inorganic matrix (mostly calcium hydroxyapatite crystals) and 35% of organic matrix (type I collagen, proteoglycans, and bound water) [20]. While the inorganic matrix is characterized by a high rigidity, a high resistivity, and an elastic behavior, the organic matrix is deformable thereby providing the tissue with tensile strength. Due to the combination of these two materials, bone tissue is simultaneously deformable and rigid [21]. The solid phase creates a shell for the bone marrow, which is the viscoelastic component. The bone marrow on the other hand has a double function. It provides nutriments to the solid phase allowing higher regenerative rate and is able, due to its viscoelastic properties, to spread the dynamics of an impulsive action, reducing the risk of fractures due to impacts [22]. Bone tissue is composed of both trabecular and cortical bone phases. Cortical bone covers the whole surface of the bone. It is compact, dense, and characterized by overlapped and parallel lamellae, which provide a large resistivity [20]. Trabecular bone is the inner compartment of bone tissue. It is composed of 25% of bone and 75% of marrow [23]. At the microstructural level, trabecular bone appears as a complex 3D network of interconnected trabeculae rods and plates responsible for tissue resistance to loading forces. The bone inner architecture is an important contributor to bone strength independent of bone mass [20]. It is characterized by a high porosity so that trabecular bone is lighter and less dense than cortical bone. In fact, cortical bone mainly works in compression while trabecular bone principally works in flexion and torsion reaching a higher area under the stress–strain curve [23].

Bone is actually a dynamic porous structure and this porosity can change as a result of pathological processes but also as an adaptive response to mechanical or physiological stimuli. This change in both cortical and trabecular bone porosity can strongly affect the corresponding mechanical properties [23].

2. MRI Based Approach

A non-invasive alternative to DXA and qCT could be MRI. Over the last two decades, a large number of studies have intended to assess bone microstructure using MRI. The initial investigations have been performed using T1-weighted spin echo sequences characterized by short TR (<1200 ms) and short TE (<25 ms) in distal radius and calcaneus [16][24][25][26]. Due to technical advances, tibiae [17][27][28], spine [24][29], and proximal femur [18][30][31][32] have been investigated. MRI of trabecular microstructure can be obtained by imaging the marrow phase inside the bone segment, which appears as a hyperintense signal in conventional MR images. Using higher field MRI, i.e., 3T one can expect an increased signal to noise ratio (SNR), which can be translated either in a reduced acquisition time or an increased image resolution. Over the last decades, due to the higher availability of high-field (HF) MRI scanners, a large number of studies have been dedicated to the MRI assessment of osteoporosis [17][18][30][33][28][32][31]. Very recently, clinical FDA and CE-approved ultra-high field (i.e., 7T UHF) MRI scanners with announced MSK applications have become available. Their clinical availability is still poor and the coming results will be of utmost importance to decide about the future of UHF MRI for clinical purposes.

Using MRI, the most common extrapolated features are the bone volume fraction (BVF), the trabecular thickness (Tb.Th), spacing (Tb.Sp), and number (Tb.N) [18][33].

2.1. Technical Considerations for Clinical Usefulness

A signal to noise ratio (SNR) of 10 has been reported as the minimum value for the investigation of bone microarchitecture [34]. The scan time considered acceptable for clinical examination has to range between 10 and 15 min. As a result the minimum voxel size, which has been obtained at 1.5T was between 0.135 and 0.250 mm while the slice thickness was between 0.3 and 1.5 mm. One has to keep in mind that SNR would be higher for superficial anatomical sites (radius or calcaneus compared to deeper anatomical sites, e.g., proximal femur) leading to higher resolution or shorter acquisition time. Moreover, SNR can be increased at higher field strengths and/or using multichannel coils [34][35][36][37].

MRI pulse sequences such as gradient recalled echo (GRE) and spin echo (SE) have also been tested at different field strengths [17][32][38]. It has been shown that SE sequences were less susceptible to partial volume effects as compared to GRE sequences and that GRE were more sensitive to trabecular broadening than SE. These results indicate that SE sequences would provide more accurate results regarding trabecular characteristics [17][38]. However, the use of these pulse sequences might be problematic using ultra-high field (UHF) MRI considering power-deposition issues.

A list of the main literature references, scanned regions, sequences, and principal MRI setup parameters is reported in Table 1.

Table 1. List of the main magnetic resonance imaging (MRI) parameters and sequences.

Anatomical Site	Clinical History	Specimen /Patient	Acq. Time	Sl. Thickness [mm] [mm]	Pix. Size [mm]	FOV [mm]	Sequence	Main Field	N°	Reference
distal radii	type 2 diabetes	patient	12 min 9 s	1	0.195 × 0.195	100 × 100	FSE	1T	[39]	Pritchard et al.
calcaneus	osteoporotic hip fractures	patient	15 min 15 s	0.5	0.195 × 0.195	100 × 100	GE	1.5T	[26]	Link et al.
distal radii	healthy	patient	16 min 25 s	0.5	0.156 × 0.156	80 × 45	3D FLASE	1.5T	[36]	Techawiboonwong et al.
distal radii	healthy	patient	3 min 15 s	0.5	0.156 × 0.156	80 × 45	3D SSFP	1.5T	[36]	Techawiboonwong et al.
distal radii	NA	specimen	15 min	0.3	0.156 × 0.156	80	GE	1.5T	[13]	Majumdar et al.
lumbar spine	osteoporotic	patient	16 min	0.7	0.156 × 0.156	80 × 80	GE	1.5T	[24]	Majumdar et al.
distal radii	hip fractures	patient	NA	0.5	0.156 × 0.156	80 × 80	GE	1.5T	[16]	Majumdar et al.
distal radii	NA	specimen	58 min (1) 16 min (2)	0.3 (1) 0.9 (2)	0.153 × 0.153	49×78	SE	1.5T	[40]	Link et al.
prox. femur	NA	specimen	74 min (1) 27 min (2)	0.3 (1) 0.9 (2)	0.195 × 0.195	75 × 100	SE	1.5T	[41]	Link et al.
prox. femur	healthy	patient	6 min 12 s	1.5	0.234 × 0.234	NA	3D FIESTA	1.5T	[32]	Krug et al.

distal tibiae	NA	specimen	40 min	0.16	0.160 × 0.160	70 × 63	3D FLASE	1.5T	[42]	Rajapakse et al.
lumbar spine	NA	specimen	15 min 23 s	0.41	0.137 × 0.137	70 × 64 × 13	3D FLASE	1.5T	[29]	Rajapakse et al.
distal radii(1) and distal tibiae(2)	osteopenic and osteoporotic	patient	12 min (1) 16 min (2)	0.4	0.137 × 0.137	70 × 40(1) 70 × 50(2)	3D FLASE	1.5T	[25]	Ladinsky et al.
distal femur	cerebral palsy (children)	patient	9 min 52 s	0.7	0.175 × 0.175	90	Gradient Echo	1.5T	[43]	Modlesky et al.
distal radii(1) and distal tibiae(2)	osteoporotic	patient	12 min (1) 16 min (2)	0.41	0.137 × 0.137	70 × 40 × 13 (1) 70 × 50 × 13 (2)	3D FLASE	1.5T	[44]	Rajapakse et al.
prox. femur	NA	specimen	18 min 55 s	1.1	0.21 × 0.21	120	TSE	3T	[31]	Soldati et al.
prox. femur	healthy	patient	12 min 43 s	1.5	0.234 × 0.235	NA	3D FIESTA	3T	[32]	Krug et al.
distal radii, distal tibiae	NA	specimen	< 10 min	0.5	0.156 × 0.156	NA	GE	3T	[38]	Krug et al.
distal radii, distal tibiae	NA	specimen	< 10 min	0.5	0.156 × 0.156	NA	SE	3T	[38]	Krug et al.
distal tibiae	osteoporotic	patient	15 min	0.41	0.137 × 0.137	70 × 64 × 13	3D FLASE	3T	[28]	Zhang et al.

References

1. Vos, T.; Flaxman, A.D.; Naghavi, M.; Lozano, R.; Michaud, C.; Ezzati, M.; Shibuya, K.; Salomon, J.A.; Abdalla, S.; Aboyans, V.; et al. Years Lived with Disability (YLDs) for 1160 Sequelae of 289 Diseases and Injuries 1990–2010: A Systematic Analysis for the Global Burden of Disease Study 2010. Lancet 2012, 380, 2163–2196, doi:10.1016/S0140-6736(12)61729-2.
2. Lim, S.S.; Vos, T.; Flaxman, A.D.; Danaei, G.; Shibuya, K.; Adair-Rohani, H.; AlMazroa, M.A.; Amann, M.; Anderson, H.R.; Andrews, K.G.; et al. A Comparative Risk Assessment of Burden of Disease and Injury Attributable to 67 Risk Factors and Risk Factor Clusters in 21 Regions, 1990–2010: A Systematic Analysis for the Global Burden of Disease Study 2010. The Lancet 2012, 380, 2224–2260, doi:10.1016/S0140-6736(12)61766-8.
3. Murray, C.J.L. Disability-Adjusted Life Years (DALYs) for 291 Diseases and Injuries in 21 Regions, 1990–2010: A Systematic Analysis for the Global Burden of Disease Study 2010. Lancet 2012, 380, 27.
4. Woolf, A.D. Global Burden of Osteoarthritis and Musculoskeletal Diseases. BMC Musculoskelet. Disord. 2015, 16, S3, 1471-2474-16-S1–S3 , doi:10.1186/1471-2474-16-S1-S3.
5. Johnell, O.; Kanis, J.A. An Estimate of the Worldwide Prevalence and Disability Associated with Osteoporotic Fractures. Osteoporos. Int. 2006, 8 , 1726–1733 .
6. Odén, A.; McCloskey, E.V.; Kanis, J.A.; Harvey, N.C.; Johansson, H. Burden of High Fracture Probability Worldwide: Secular Increases 2010–2040. Osteoporos. Int. 2015, 26, 2243–2248, doi:10.1007/s00198-015-3154-6.
7. Burge, R.; Dawson-Hughes, B.; Solomon, D.H.; Wong, J.B.; King, A.; Tosteson, A. Incidence and Economic Burden of Osteoporosis-Related Fractures in the United States, 2005–2025. J. Bone Miner. Res. 2007, 22, 465–475, doi:10.1359/jbmr.061113.
8. Van Oostwaard, M. Osteoporosis and the Nature of Fragility Fracture: An Overview. In Fragility Fracture Nursing; Hertz, K.,Santy-Tomlinson, J., Eds.; Perspectives in Nursing Management and Care for Older Adults; Springer International Publishing:Cham, Switzerland, 2018; pp. 1–13; ISBN 978-3-319-76680-5.
9. Nayak, S.; Edwards, D.L.; Saleh, A.A.; Greenspan, S.L. Systematic Review and Meta-Analysis of the Performance of Clinical Risk Assessment Instruments for Screening for Osteoporosis or Low Bone Density. Osteoporos. Int. 2015, 26, 1543–1554, doi:10.1007/s00198-015-3025-1.
10. Humadi, A.; Alhadithi, R.; Alkudiari, S. Validity of the DEXA Diagnosis of Involutional Osteoporosis in Patients with Femoral Neck Fractures. Indian J. Orthop. 2010, 44, 73, doi:10.4103/0019-5413.58609.
11. Sharma, A.K.; Toussaint, N.D.; Elder, G.J.; Masterson, R.; Holt, S.G.; Robertson, P.L.; Ebeling, P.R.; Baldock, P.; Miller, R.C.; Rajapakse, C.S. Magnetic Resonance Imaging Based Assessment of Bone Microstructure as a Non-Invasive Alternative to Histomorphometry in Patients with Chronic Kidney Disease. Bone 2018, 114, 14–21, doi:10.1016/j.bone.2018.05.029.
12. Boutroy, S.; Bouxsein, M.L.; Munoz, F.; Delmas, P.D. In Vivo Assessment of Trabecular Bone Microarchitecture by High-Resolution Peripheral Quantitative Computed Tomography. J. Clin. Endocrinol. Metab. 2005, 90, 6508–6515, doi:10.1210/jc.2005-1258.
13. Majumdar, S.; Newitt, D.; Mathur, A.; Osman, D.; Gies, A.; Chiu, E.; Lotz, J.; Kinney, J.; Genant, H. Magnetic Resonance Imaging of Trabecular Bone Structure in the Distal Radius: Relationship with X-Ray Tomographic Microscopy and Biomechanics. Osteoporos. Int. 1996, 6, 376–385, doi:10.1007/BF01623011.
14. Seifert, A.C.; Li, C.; Rajapakse, C.S.; Bashoor-Zadeh, M.; Bhagat, Y.A.; Wright, A.C.; Zemel, B.S.; Zavaliangos, A.; Wehrli, F.W. Bone Mineral 31 P and Matrix-Bound Water Densities Measured by Solid-State 31 P and 1 H MRI: BONE DENSITY QUANTIFICATION BY MRI. NMR Biomed. 2014, 27, 739–748, doi:10.1002/nbm.3107.
15. Karamat, M.I.; Darvish-Molla, S.; Santos-Diaz, A. Opportunities and Challenges of 7 Tesla Magnetic Resonance Imaging: A Review. Crit Rev. Biomed. Eng. 2016, 44, 73–89, doi:10.1615/CritRevBiomedEng.2016016365.
16. Majumdar, S.; Link, T.M.; Augat, P.; Lin, J.C.; Newitt, D.; Lane, N.E.; Genant, H.K. Trabecular Bone Architecture in the Distal Radius Using Magnetic Resonance Imaging in Subjects with Fractures of the Proximal Femur. Osteoporos. Int.

prox. femur; distal tibia	fragility fractured	patient	25 min	1.5	0.234 × 0.234	120 × 120	FLASH	3T	[30]	Chang et al.
prox. femur	longterm glucocorticoid	patient	30 s 15 min 18 s	1.5	0.234 × 0.234	100	FLASH	3T	[31]	Chang et al.
distal radii	HR-pQCT cancer	patient	7 min	0.34	0.170 × 0.170	65	GE	3T	[46]	Baum et al.
distal femur	osteoarthritis	patient	9 min 18 s	1	0.180 × 0.180	100	3D B-FFE	3T	[47]	Liu et al.
prox. tibia	osteoarthritis	patient	3 min	2.8	0.230 × 0.230	120 × 123	SE	3T	[48]	MacKey et al.
prox. tibia, distal femur	osteoarthritis	patient	NA	1	0.195 × 0.195	100	FIESTA-c	3T	[49]	Chiba et al.
prox. tibia, distal femur	osteoarthritis	patient	NA	1	0.195 × 0.195	160	SPGR	3T	[49]	Chiba et al.
distal tibiae	NA	specimen	7 min	0.41	0.137 × 0.137	70 × 53 × 13	3D FLASE	3T	[19]	Rajapakse et al.
prox. femur	NA	specimen	16 min 45 s	1.5	0.13 × 0.13	120	TSE	7T	[50]	Rajapakse et al.
prox. femur	NA	specimen	37 min 36 s	0.5	0.170 × 0.170	140 × 140	GRE	7T	[33]	Guenoun et al.
distal tibiae	healthy	patient	19 min 10 s	0.5	0.156 × 0.156	NA	SE	7T	[17]	Krug et al.
distal tibiae	healthy	patient	18 min 25 s	0.5	0.156 × 0.157	NA	FP	7T	[17]	Krug et al.

1. Krug, R.; Carballido-Gamio, J.; Banerjee, S.; Burghardt, A.J.; Link, T.M.; Majumdar, S. In Vivo Ultra-High-Field Magnetic Resonance Imaging of Trabecular Bone Microarchitecture at 7 T. J. Magn. Reson. Imaging 2008, 27, 854–859, doi:10.1002/jmri.21325.
2. Chang, G.; Honig, S.; Liu, Y.; Chen, C.; Chu, K.K.; Rajapakse, C.S.; Egol, K.; Xia, D.; Saha, P.K.; Regatte, R.R. 7 Tesla MRI of Bone Microarchitecture Discriminates between Women without and with Fragility Fractures Who Do Not Differ by Bone Mineral Density. J. Bone Miner. Metab 2015, 33, 285–293, doi:10.1007/s00774-014-0588-4.
3. Rajapakse, C.S.; Kobe, E.A.; Batzdorf, A.S.; Hast, M.W.; Wehrli, F.W. Accuracy of MRI-Based Finite Element Assessment of Distal Tibia Compared to Mechanical Testing. Bone 2018, 108, 71–78, doi:10.1016/j.bone.2017.12.023.
4. Wang, X.; Nyman, J.S.; Dong, X.; Leng, H.; Reyes, M. Fundamental Biomechanics in Bone Tissue Engineering. Synth. Lect. Tissue Eng. 2010, 2, 1–225, doi:10.2200/S00246ED1V01Y200912TIS004.
5. Fratzl, P.; Gupta, H.S. Nanoscale Mechanisms of Bone Deformation and Fracture. In Handbook of Biomineralization; Buehlein, E., Ed.; Wiley-VCH Verlag GmbH: Weinheim, Germany, 2007; pp. 397–414, ISBN 978-3-527-61944-3.
6. Nyman, J.S.; Roy, A.; Shen, X.; Acuna, R.L.; Tyler, J.H.; Wang, X. The Influence of Water Removal on the Strength and Toughness of Cortical Bone. J. Biomech. 2006, 39, 931–938, doi:10.1016/j.jbiomech.2005.01.012.
7. Cowin, S.C. Bone Poroelasticity. J. Biomech. 1999, 32, 217–238, doi:10.1016/s0021-9290(98)00161-4.
8. Majumdar, S.; Genant, H.K.; Grampp, S.; Newitt, D.C.; Truong, V.-H.; Lin, J.C.; Mathur, A. Correlation of Trabecular Bone Structure with Age, Bone Mineral Density, and Osteoporotic Status: In Vivo Studies in the Distal Radius Using High Resolution Magnetic Resonance Imaging. J. Bone Miner. Res. 1997, 12, 111–118, doi:10.1359/jbmr.1997.12.1.111.
9. Ladinsky, G.A.; Vasilic, B.; Popescu, A.M.; Wald, M.; Zemel, B.S.; Snyder, P.J.; Loh, L.; Song, H.K.; Saha, P.K.; Wright, A.C.; et al. Trabecular Structure Quantified With the MRI-Based Virtual Bone Biopsy in Postmenopausal Women Contributes to Vertebral Deformity Burden Independent of Areal Vertebral BMD. J. Bone Miner. Res. 2007, 23, 64–74, doi:10.1359/jbmr.070815.
10. Link, T.M.; Majumdar, S.; Augat, P.; Lin, J.C.; Newitt, D.; Lu, Y.; Lane, N.E.; Genant, H.K. In Vivo High Resolution MRI of the Calcaneus: Differences in Trabecular Structure in Osteoporosis Patients. J. Bone Miner Res. 1998, 13, 1175–1182, doi:10.1359/jbmr.1998.13.7.1175.
11. Zhang, X.H.; Liu, X.S.; Vasilic, B.; Wehrli, F.W.; Benito, M.; Rajapakse, C.S.; Snyder, P.J.; Guo, X.E. In Vivo MMRI-Based Finite Element and Morphological Analyses of Tibial Trabecular Bone in Eugonadal and Hypogonadal Men Before and After Testosterone Treatment. J. Bone Miner Res. 2008, 23, 1426–1434, doi:10.1359/jbmr.080405.
12. Zhang, H.; Magland, J.F.; Rajapakse, C.S.; Bhagat, Y.A.; Wehrli, F.W. Potential of in Vivo MRI-Based Nonlinear Finite-Element Analysis for the Assessment of Trabecular Bone Post-Yield Properties. Med. Phys. 2013, 40, 052303, doi:10.1118/1.4802085.
13. Rajapakse, C.S.; Leonard, M.B.; Bhagat, Y.A.; Sun, W.; Magland, J.F.; Wehrli, F.W. Micro–MR Imaging–Based Computational Biomechanics Demonstrates Reduction in Cortical and Trabecular Bone Strength after Renal Transplantation. Radiology 2012, 262, 912–920, doi:10.1148/radiol.11111044.
14. Chang, G.; Deniz, C.M.; Honig, S.; Rajapakse, C.S.; Egol, K.; Regatte, R.R.; Brown, R. Feasibility of Three-Dimensional MRI of Proximal Femur Microarchitecture at 3 Tesla Using 26 Receive Elements without and with Parallel Imaging: 3D MRI of Proximal Femur Microarchitecture. J. Magn. Reson. Imaging 2014, 40, 229–238, doi:10.1002/jmri.24345.
15. Chang, G.; Rajapakse, C.S.; Regatte, R.R.; Babb, J.; Saxena, A.; Belmont, H.M.; Honig, S. 3 Tesla MRI Detects Deterioration in Proximal Femur Microarchitecture and Strength in Long-Term Glucocorticoid Users Compared with Controls: Changes in Proximal Femur Microarchitecture in GIO. J. Magn. Reson. Imaging 2015, 42, 1489–1496, doi:10.1002/jmri.24927.
16. Krug, R.; Banerjee, S.; Han, E.T.; Newitt, D.C.; Link, T.M.; Majumdar, S. Feasibility of in Vivo Structural Analysis of High-Resolution Magnetic Resonance Images of the Proximal Femur. Osteoporos. Int. 2005, 16, 1307–1314, doi:10.1007/s00198-005-1907-3.
17. Guenoun, D.; Pithioux, M.; Souplet, J.-C.; Guis, S.; Le Corroller, T.; Fouré, A.; Pauly, V.; Mattei, J.-P.; Bernard, M.; Guye, M.; et al. Assessment of Proximal Femur Microarchitecture Using Ultra-High Field MRI at 7 Tesla. Diagn. Interv. Imaging 2020, 101, 45–53, doi:10.1016/j.diii.2019.06.013.
18. Wehrli, F.W. Structural and Functional Assessment of Trabecular and Cortical Bone by Micro Magnetic Resonance Imaging. J. Magn. Reson. Imaging 2007, 25, 390–409, doi:10.1002/jmri.20807.

vertebrae (1 axial, 2 sagittal)	NA	specimen	34 min (1) 51 min (2)	0.4 (1) 0.5 (2)	0.170 × 0.170	140 × 140	GRE	7T	[51]	Guenoun et al.
distal femur	fragility fractured	patient	7 min 9 s	1	0.234 × 0.234	120	FLASH	7T	[18]	Chang et al.
femurs, tibiae, vertebrae	NA	specimen	120 min	0.05	0.05 × 0.05	6.4 × 6.4 × 25.6	SE	9.4T	[52]	Rajapakse et al.

2.2. Microstructure Investigation

In the majority of MRI literature, the morphological parameters that are reported are BVF, Tb.Th, Tb.Sp, and Tb.N [32][38][19]. In addition, some groups have proposed some other features such as an erosion index, trabecular rod- and plate-like structures, trabecular plate-to-rod ratio, trabecular isolation, and fractal lacunarity [39][40].

These microarchitectural parameters have been generated from the post-processing of both 2D and 3D images. The corresponding analyses were performed in binarized images or in original grey level intensities. All these approaches have tried to take into account partial volume effects occurring given the poor resolution of MRI as compared to the trabeculae dimension [33][41][42]. So far, no standard reference has been suggested.

Studies performed at different MRI field strength in postmenopausal woman with fragility fractures have illustrated microstructural alterations (reduced BVF and increased Tb.Sp) whereas DXA T-scores were unchanged. In a study conducted in distal radii at 1.5T, Kijowsky et al. showed that postmenopausal woman had a slightly lower (−9%) bone volume fraction and a higher erosion index (+17%) compared to controls [43]. Krug et al. in a study conducted on the proximal femur of six healthy males and females using both 1.5T and 3T MRI showed good correlation (r up to 0.86) between structural parameters obtained from the two different field strengths. However, they reported that bone structure of the proximal femur was substantially better depicted at 3T than 1.5T [32]. Microstructure alterations have been reported in a large variety of cases including chronic kidney disease (CKD) [11][53], HIV-infection [44], glucocorticoid-induced osteoporosis [31], or disuse osteoporosis [45].

In a 3T MRI study conducted in distal tibiae of 20 patients with CKD, Ruderman et al. reported trabecular deterioration together with reduced cortical thickness [53]. Moreover, a study conducted on 30 patients affected by end stage renal disease (ESRD), it has been shown that Tb.N, Tb.Th, and whole bone stiffness were significantly lower ($p < 0.01$) is ESRD compared to controls [46]. A similar study conducted on distal tibiae of 11 kidney transplant recipient patients have highlightened post-transplant deterioration in trabecular bone quality [47]. In a study conducted in proximal femurs at 3T, glucocorticoid treated patients had a largely reduced (−50.3%) Tb.N, trabecular plate-to-rod ratio (−20.1%), and a largely increased (+191%) Tb.Sp [31]. Patients with a disuse osteoporosis displayed similar anomalies for BVF (−30%), Tb.N (−21%), Tb.Th (−12%), and Tb.Sp (+48%) [45]. Chang et al. [18] further supported and extended these results in a study conducted in distal femur at 7T. In 31 subjects with fragility fractures, they reported a lower BVF (−3%), Tb.N (−6%), and erosion index (−6%). Moreover, in a 7T MRI study conducted in the distal radius of 24 women, Griffin et al. reported a trabecular bone microarchitecture gradient with an overall higher quality (+123% BVF, +16% Tb.N) distally (epiphysis) than proximally (diaphysis) [48].

Ultra-high field MRI can provide images with a smaller pixel size (0.156 mm × 0.156 mm) as compared to the resolution achieved at lower field strength (0.234 mm × 0.234 mm for example at 3T [17][32]). In a dual 3T-7T study conducted in distal tibiae of 10 healthy volunteers, Krug et al. reported that metrics computed at higher field strength were different than those quantified from 3T MR images. More specifically, UHF measurements illustrated increased BVF (+22%) and Tb.Th (+25%) whereas Tb.Sp (−21%) and Tb.N (−4%) were both decreased [88]. These results suggest a higher discriminative power of UHF MRI for trabecular features.

35. Brown, R.; Cheng, Y.; Thompson, M.; Haacke, E.M.; Venkatesan, R. Magnetic Resonance Imaging: Physical Principles and Sequence Design; John Wiley & Sons: Hoboken, NJ, USA , 2014; ISBN 1-118-63397-0.
36. Techawiboonwong, A.; Song, H.K.; Magland, J.F.; Saha, P.K.; Wehrli, F.W. Implications of Pulse Sequence in Structural Imaging of Trabecular Bone. J. Magn. Reson. Imaging 2005, 22, 647–655, doi:10.1002/jmri.20432.
37. Chang, G.; Boone, S.; Martel, D.; Rajapakse, C.S.; Hallyburton, R.S.; Valko, M.; Honig, S.; Regatte, R.R. MRI Assessment of Bone Structure and Microarchitecture: Bone Structure and Microarchitecture. J. Magn. Reson. Imaging 2017, 46, 323–337, doi:10.1002/jmri.25647.
38. Krug, R.; Carballido-Gamio, J.; Burghardt, A.J.; Kazakia, G.; Hyun, B.H.; Jobke, B.; Banerjee, S.; Huber, M.; Link, T.M.; Majumdar, S. Assessment of Trabecular Bone Structure Comparing Magnetic Resonance Imaging at 3 Tesla with High-Resolution Peripheral Quantitative Computed Tomography Ex Vivo and in Vivo. Osteoporos. Int. 2008, 19, 653–661, doi:10.1007/s00198-007-0495-9.
39. Pritchard, J.M.; Giangregorio, L.M.; Atkinson, S.A.; Beattie, K.A.; Inglis, D.; Ioannidis, G.; Gerstein, H.; Punthakee, Z.; Adachi, J.D.; Papaioannou, A. Changes in Trabecular Bone Microarchitecture in Postmenopausal Women with and without Type 2 Diabetes: A Two Year Longitudinal Study. BMC Musculoskelet. Disord. 2013, 14, 114, doi:10.1186/1471-2474-14-114.
40. Link, T.M.; Vieth, V.; Stehling, C.; Lotter, A.; Beer, A.; Newitt, D.; Majumdar, S. High-Resolution MRI vs Multislice Spiral CT: Which Technique Depicts the Trabecular Bone Structure Best? Eur. Radiol. 2003, 13, 663–671, doi:10.1007/s00330-002-1695-5.
41. Link, T.M.; Vieth, V.; Langenberg, R.; Meier, N.; Lotter, A.; Newitt, D.; Majumdar, S. Structure Analysis of High Resolution Magnetic Resonance Imaging of the Proximal Femur: In Vitro Correlation with Biomechanical Strength and BMD. Calcif. Tissue Int. 2003, 72, 156–165, doi:10.1007/s00223-001-2132-5.
42. Rajapakse, C.S.; Magland, J.F.; Wald, M.J.; Liu, X.S.; Zhang, X.H.; Guo, X.E.; Wehrli, F.W. Computational Biomechanics of the Distal Tibia from High-Resolution MR and Micro-CT Images. Bone 2010, 47, 556–563, doi:10.1016/j.bone.2010.05.039.
43. Modlesky, C.M.; Subramanian, P.; Miller, F. Underdeveloped Trabecular Bone Microarchitecture Is Detected in Children with Cerebral Palsy Using High-Resolution Magnetic Resonance Imaging. Osteoporos. Int. 2008, 19, 169–176, doi:10.1007/s00198-007-0433-x.
44. Rajapakse, C.S.; Phillips, E.A.; Sun, W.; Wald, M.J.; Magland, J.F.; Snyder, P.J.; Wehrli, F.W. Vertebral Deformities and Fractures Are Associated with MRI and PQCT Measures Obtained at the Distal Tibia and Radius of Postmenopausal Women. Osteoporos. Int. 2014, 25, 973–982, doi:10.1007/s00198-013-2569-1.
45. Soldati, E.; Bendahan, D.; Pithioux, M.; Vicente, J. MRI Assessment of Bone Microarchitecture in Human Bone Samples: The Issue of Air Bubbles Artefacts. Bone Rep. 2020, 13, 100541, doi:10.1016/j.bonr.2020.100541.
46. Baum, T. Use of MR-Based Trabecular Bone Microstructure Analysis at the Distal Radius for Osteoporosis Diagnostics: A Study in Post-Menopausal Women with Breast Cancer and Treated with Aromatase Inhibitor. CCMBM 2016, doi:10.11138/ccmbm/2016.13.1.029.
47. Liu, C.; Liu, C.; Ren, X.; Si, L.; Shen, H.; Wang, Q.; Yao, W. Quantitative Evaluation of Subchondral Bone Microarchitecture in Knee Osteoarthritis Using 3T MRI. BMC Musculoskelet. Disord. 2017, 18, 496, doi:10.1186/s12891-017-1865-x.
48. MacKay, J.W.; Murray, P.J.; Kasmai, B.; Johnson, G.; Donell, S.T.; Toms, A.P. Subchondral Bone in Osteoarthritis: Association between MRI Texture Analysis and Histomorphometry. Osteoarthr. Cartil. 2017, 25, 700–707, doi:10.1016/j.joca.2016.12.011.
49. Chiba, K.; Uetani, M.; Kido, Y.; Ito, M.; Okazaki, N.; Taguchi, K.; Shindo, H. Osteoporotic Changes of Subchondral Trabecular Bone in Osteoarthritis of the Knee: A 3-T MRI Study. Osteoporos. Int. 2012, 23, 589–597, doi:10.1007/s00198-011-1585-2.
50. Soldati, E.; Pithioux, M.; Vicente, J.; Bendahan, D. Trabecular Bone Microarchitecture: A Comparative Analysis between High Field, Ultra High Field MRI and X-Ray Micro CT in Humans Anatomical Samples. Bone Rep. 2020, 13, 100542, doi:10.1016/j.bonr.2020.100542.
51. Guenoun, D.; Fouré, A.; Pithioux, M.; Guis, S.; Le Corroller, T.; Mattei, J.-P.; Pauly, V.; Guye, M.; Bernard, M.; Chabrand, P.; et al. Correlative Analysis of Vertebral Trabecular Bone Microarchitecture and Mechanical Properties: A Combined Ultra-High Field (7 Tesla) MRI and Biomechanical Investigation. SPINE 2017, 42, E1165–E1172, doi:10.1097/BRS.0000000000002163.
52. Rajapakse, C.S.; Magland, J.; Zhang, X.H.; Liu, X.S.; Wehrli, S.L.; Guo, X.E.; Wehrli, F.W. Implications of Noise and Resolution on Mechanical Properties of Trabecular Bone Estimated by Image-Based Finite-Element Analysis. J. Orthop. Res. 2009, 27, 1263–1271, doi:10.1002/jor.20877.

2.3. Microstructure vs. DXA

In a study conducted in 32 postmenopausal women, Kang et al. showed a good correlation between DXA-based BMD and MRI T2 and T2 * in calcaneus (r = −0.8, $p < 0.001$) and spine (r = −0.53, $p = 0.002$) [50]. Similar results have been reported for the femoral neck [65,90] with a good correlation (r = 0.74, $p < 0.001$) between DXA-based BMD and T2 * values [52]. T2 * relaxation time illustrates the susceptibility differences between trabecular and bone marrow leading to signal loss due to magnetic field inhomogeneities. MRI-derived T2 * has been shown to correlate with DXA results in several anatomical areas such as calcaneus, distal radius, and Ward's area in the femoral neck [54][55]. Based on T2 * measurements, Schmeel et al. reported a significant difference between benign and malignant neoplastic vertebral compression fractures (VCFs). A 72% diagnostic accuracy was computed [56]. Furthermore, a strong negative correlation was found between the pelvic bone marrow adipose tissue (BMAT) calculated in 56 healthy women using MRI and the corresponding DXA-based BMD (r = −0.646, $p < 0.001$) [57]. The negative correlation indicates that patients with decreased bone mineral density are characterized by an increased fat content in bone marrow. [57][58][59]

Based on highly resolved MR images (0.150–0.300 mm in-plane pixel size), Chang et al. showed a lack of significant correlation between DXA-computed BMD T-scores and MRI computed microarchitectural parameters in the femoral neck in both controls and glucocorticoid-treated patients [31][60]. Similar results were also reported more recently in subchondral tibiae [61], proximal femurs [33][42], vertebrae [62], and on patients affected by diabetes [63][64]. Guenoun et al. reported that the combination of BVF and BMD was able to improve the prediction of the failure stress (from $r^2 = 0.384$ for BMD alone to $r^2 = 0.414$). All the presented results suggest that although density and structure metrics illustrate bone quality, microarchitectural parameters provide additional information regarding skeletal fragility.

2.4. Voxel Size and Microstructure

Results from the literature showed that image resolution is a key parameter for the assessment of bone microarchitecture. Importantly, a distinction must be made between in-plane and through-planes resolution. For specific oriented plane (mostly perpendicular to the trabecular), an in-plane MRI pixel size in the same order of magnitude than Tb.Th dimension is enough to measure morphological parameters similar to those extrapolated using gold standard method and so both ex vivo (μCT) [42][65] and in vivo (HR-pQCT) [33]. If one intends to assess bone microstructure using small isovolumetric voxels (0.15 mm), close to the actual thickness of the trabeculae, with an acceptable SNR, acquisition times would exceed the in vivo acceptable duration. One can increase the SNR and reduce the acquisition time with an increased slice thickness while keeping the plane pixel size constant. Accordingly, the radius morphological parameters computed from similar in-plane pixel sizes and different slice thicknesses (0.156 mm × 0.156 mm × 0.3 mm [13], 0.156 mm × 0.156 mm × 0.5 mm [16][66], 0.156 mm × 0.156 mm × 0.7 mm [24], and 0.153 mm × 0.153 mm × 0.9 mm [67]) were comparable. In fact, the bone inner microarchitecture appeared to be a mixture of oriented plates- and rod-like structures. The parallel trabecular plates structures are separated by bone marrow and are perpendicular to the coronal plane [68]. On that basis, increasing the in-plane pixel size should provide more accurate results independently of the slice thickness. As reported by Mulder et al., the calculated volume of ellipsoid at high resolution (0.1 mm × 0.1 mm) is independent from the anisotropy factor but related to the orientation [69].

Different studies performed in distal radii at 1.5T, using similar in-plane pixel size and using different slice thicknesses above 0.3 mm, reported comparable morphological results [13][16][43]. However, in a study conducted by Majumdar et al. in 39 distal radii specimens acquired using 1.5T MRI and contact radiograph, 0.9-mm thick MR images performed better than those obtained from 0.3-mm images. This was explained with the significantly higher SNR (18.2 in 0.9-mm thick images and 9.3 in 0.3-mm sections) [67]. Similar results were obtained in vivo in distal radii scanned at 1.5T (0.156 mm × 0.156 mm × 0.5 mm) with an acceptable SNR around 10 [36]. Moreover, wrists and distal tibiae scanned in patients using 1.5T with pixel sizes in the same range of trabecular thickness (0.156 mm × 0.156 mm × 0.410 mm [25] and 0.137 mm × 0.137 mm × 0.410 mm [70]) reporting lower acquisition time for wrist (12 min) than for tibiae (16 min) and good image quality in both anatomical regions. In a second study conducted by Majumdar et al., 31 cadaveric proximal femurs were scanned at 1.5T with an in-plane pixel size of 0.195 × 0.195 and comparing two different slice thicknesses (0.9 and 0.3 mm). The SNR achieved was 25.2 and 13.8 for the larger and smaller slice thickness respectively. The corresponding acquisition times were very long (27:19 and 73:14 min), i.e., much longer than what could be accepted in clinics [71].

The knee articulation has also been assessed in the study of Rajapakse et al., 17 distal tibiae specimens were scanned at 3T (0.137 mm × 0.137 mm × 0.410 mm) in 7 min [19]. These results where extended in vivo by Zhang et al., in the distal tibiae of 20 postmenopausal women with osteoporosis. The scanning time using 3T MRI (0.137 mm × 0.137 mm × 0.410 mm) was less than 15 min [28]. Krug et al. further confirmed these results in a study comparing 3T MRI (0.156 mm × 0.156 mm × 0.5 mm) and X-ray based techniques both ex vivo (5 tibiae and 3 radii) and in vivo (5 radii and 6 tibiae). While the scanning time was less than 10 min, correlations were reported between both methods and so for the whole set of

53. Ruderman, I.; Rajapakse, C.S.; Opperman, A.; Robertson, P.L.; Masterson, R.; Tiong, M.K.; Toussaint, N.D. Bone Microarchitecture in Patients Undergoing Parathyroidectomy for Management of Secondary Hyperparathyroidism. Bone Rep. 2020, 13, 100297, doi:10.1016/j.bonr.2020.100297.

54. Hipp, J.A.; Jansujwicz, A.; Simmons, C.A.; Snyder, B.D. Trabecular Bone Morphology from Micro-Magnetic Resonance Imaging. J. Bone Miner. Res. 2009, 11, 286–292, doi:10.1002/jbmr.5650110218.

55. Zaia, A.; Rossi, R.; Galeazzi, R.; Sallei, M.; Maponi, P.; Scendoni, P. Fractal Lacunarity of Trabecular Bone in Vertebral MRI to Predict Osteoporotic Fracture Risk in Over-Fifties Women. The LOTO Study. BMC Musculoskelet. Disord. 2021, 22, 108, doi:10.1186/s12891-021-03966-7.

56. Kijowski, R.; Tuite, M.; Kruger, D.; Munoz Del Rio, A.; Kleerekoper, M.; Binkley, N. Evaluation of Trabecular Microarchitecture in Nonosteoporotic Postmenopausal Women with and without Fracture. J. Bone Miner. Res. 2012, 27, 1494–1500, doi:10.1002/jbmr.1595.

57. Kazakia, G.J.; Carballido-Gamio, J.; Lai, A.; Nardo, L.; Facchetti, L.; Pasco, C.; Zhang, C.A.; Han, M.; Parrott, A.H.; Tien, P.; et al. Trabecular Bone Microstructure Is Impaired in the Proximal Femur of Human Immunodeficiency Virus-Infected Men with Normal Bone Mineral Density. Quant. Imaging Med. Surg. 2018, 8, 5–13, doi:10.21037/qims.2017.10.10.

58. Leonard, M.B.; Wehrli, F.W.; Ziolkowski, S.L.; Billig, E.; Long, J.; Nickolas, T.L.; Magland, J.F.; Nihtianova, S.; Zemel, B.S.; Herskovitz, R.; et al. A Multi-Imaging Modality Study of Bone Density, Bone Structure and the Muscle Bone Unit in End-Stage Renal Disease. Bone 2019, 127, 271–279, doi:10.1016/j.bone.2019.05.022.

59. Sharma, A.K.; Toussaint, N.D.; Elder, G.J.; Rajapakse, C.S.; Holt, S.G.; Baldock, P.; Robertson, P.L.; Ebeling, P.R.; Sorci, O.R.; Masterson, R. Changes in Bone Microarchitecture Following Kidney Transplantation-Beyond Bone Mineral Density. Clin. Transplant. 2018, 32, e13347, doi:10.1111/ctr.13347.

60. Griffin, L.M.; Honig, S.; Chen, C.; Saha, P.K.; Regatte, R.; Chang, G. 7T MRI of Distal Radius Trabecular Bone Microarchitecture: How Trabecular Bone Quality Varies Depending on Distance from End-of-Bone: 7T MRI of Distal Radius. J. Magn. Reson. Imaging 2017, 45, 872–878, doi:10.1002/jmri.25398.

61. Agten, C.A.; Honig, S.; Saha, P.K.; Regatte, R.; Chang, G. Subchondral Bone Microarchitecture Analysis in the Proximal Tibia at 7-T MRI. Acta Radiol. 2018, 59, 716–722, doi:10.1177/0284185117732098.

62. Kang, C.; Paley, M.; Ordidge, R.; Speller, R. In Vivo MRI Measurements of Bone Quality in the Calcaneus: A Comparison with DXA and Ultrasound. Osteoporos. Int. 1999, 9, 65–74, doi:10.1007/s001980050117.

63. Chen, S.C.; Shepherd, S.; McMillan, M.; McNeilly, J.; Foster, J.; Wong, S.C.; Robertson, K.J.; Ahmed, S.F. Skeletal Fragility and Its Clinical Determinants in Children With Type 1 Diabetes. J. Clin. Endocrinol. Metab. 2019, 104, 3585–3594, doi:10.1210/jc.2019-00084.

64. Abdalrahaman, N.; McComb, C.; Foster, J.E.; Lindsay, R.S.; Drummond, R.; McKay, G.A.; Perry, C.G.; Ahmed, S.F. The Relationship between Adiposity, Bone Density and Microarchitecture Is Maintained in Young Women Irrespective of Diabetes Status. Clin. Endocrinol. 2017, 87, 327–335, doi:10.1111/cen.13410.

65. Guglielmi, G.; Selby, K.; Blunt, B.A.; Jergas, M.; Newitt, D.C.; Genant, H.K.; Majumdar, S. Magnetic Resonance Imaging of the Calcaneus: Preliminary Assessment of Trabecular Bone-Dependent Regional Variations in Marrow Relaxation Time Compared with Dual X-Ray Absorptiometry. Acad. Radiol. 1996, 3, 336–343, doi:10.1016/S1076-6332(96)80254-6.

66. Arokoski, M.H.; Arokoski, J.P.A.; Vainio, P.; Niemitukia, L.H.; Kröger, H.; Jurvelin, J.S. Comparison of DXA and MRI Methods for Interpreting Femoral Neck Bone Mineral Density. J. Clin. Densitom. 2002, 5, 289–296, doi:10.1385/JCD:5:3:289.

67. Brismar, T.B. MR Relaxometry of Lumbar Spine, Hip, and Calcaneus in Healthy Premenopausal Women: Relationship with Dual Energy X-Ray Absorptiometry and Quantitative Ultrasound. Eur. Radiol. 2000, 10, 1215–1221, doi:10.1007/s003300000438.

68. Grampp, S.; Majumdar, S.; Jergas, M.; Newitt, D.; Lang, P.; Harry, K. Genant Distal Radius: In Vivo Assessment with Quantitative MR Imaging, Peripheral Quantitative CT, and Dual X-Ray Absorptiometry. 1996, doi:10.1148/radiology.198.1.8539382.

69. Schmeel, F.C.; Luetkens, J.A.; Feißt, A.; Enkirch, S.J.; Endler, C.H.-J.; Wagenhäuser, P.J.; Schmeel, L.C.; Träber, F.; Schild, H.H.; Kukuk, G.M. Quantitative Evaluation of T2* Relaxation Times for the Differentiation of Acute Benign and Malignant Vertebral Body Fractures. Eur. J. Radiol. 2018, 108, 59–65, doi:10.1016/j.ejrad.2018.09.021.

70. Shen, W.; Chen, J.; Punyanitya, M.; Shapses, S.; Heshka, S.; Heymsfield, S.B. MRI-Measured Bone Marrow Adipose Tissue Is Inversely Related to DXA-Measured Bone Mineral in Caucasian Women. Osteoporos. Int. 2007, 18, 641–647, doi:10.1007/s00198-006-0285-9.

parameters, i.e., BVF (r = 0.83) and Tb.Sp (r = 0.7) [72]. Liu et al. also reported 3T MR images (pixel size 0.180 mm × 0.180 mm, acq. time 9:18 min) of 92 distal femurs divided in three groups (without osteoarthritis, mild osteoarthritis, and severe osteoarthritis) reporting progressively lower BVF and higher erosion index from healthy patients to those affected by severe osteoarthritis [73], extending previous results [74][75][76].

2.5. Main Magnetic Field Strength Effect

The technical advantages of moving from 1.5T to 3T or 7T MR scanners were clearly visible in the acquisition of deeper anatomical sites keeping the spatial pixel size in the same order of the trabecular thickness, the acquisition time (acq. Time), and the SNR (>10) being clinically compatible. On that basis, 7T MR scanners have been tested mostly for the acquisition of distal and proximal femur, which represent a clinical important fracture site and one of the most invalidating [77].

In a comparative study conducted in vivo in proximal femur at 1.5 and 3T, Krug et al., reported as expected a 1.6 time-SNR increase together with a corresponding contrast-to-noise ratio (CNR) increase at higher magnetic field. While the 3T images clearly showed the trabecular bone structure, the image resolution did not allow a proper trabecular morphological analysis [32]. In a more recent study in the knee joint of 16 healthy volunteers scanned at 1.5T (0.6 mm × 0.6 mm × 0.6 mm, acq. time 7:15 min) and 3T (0.5 mm × 0.5 mm × 0.5 mm, acq. time 6:51 min), Abdulaal et al. reported significantly higher SNR ($p < 0.05$) allowing a better trabecular characterization at 3T than 1.5T [78]. Moreover, 3T MRI could be used to successfully scan radii with an in-plane pixel size comparable to the trabecular thickness and an acquisition time (10 min) lower than what commonly needed at 1.5T [66][79]. Jerraya et al., on a study conducted in 50 distal radii scanned at both 3T (0.2 mm × 0.2 mm × 2.0 mm, acq. time 4:29 min) and 7T MR (0.125 mm × 0.125 mm × 2.0 mm, acq. time 3:16 min), reported a statistical significant difference of horizontal and fractal dimensions between patients with chronic wrist disease and controls [80]. A similar comparative analysis has been performed between 3T and 7T MRI (0.156 mm × 0.156 mm × 0.5 mm, acq. time lower than 10 min) and HR-pQCT. Krug et al. showed that tibial trabecular structures were over-represented at higher field strength. Due to susceptibility-induced broadening smaller trabeculae normally not visible due to partial volume effects may be emphasized at 7T [49]. Moreover, using UHF MRI (0.234 mm × 0.234 mm × 1.0 mm, acq. time 7 min), Chang et al. reported that microarchitectural parameters could discriminate between patients and controls and could detect bone deterioration in women with fragility fractures for whom BMD was normal [18]. In addition to the effects of magnetic field strength, Krug et al. also assessed the potential differences between GRE and TSE sequences at 7T. SNR was slightly higher for GRE sequences (13.2 vs. 11.9) while the bone marrow signal was more homogeneous using TSE sequences. This large homogeneity is related to a reduced susceptibility-induced broadening of the trabeculae so that the morphological analysis showed decreased BVF (−13%) and Tb.Th (−23%). These values were closer to those reported using the HR-pQCT reference method [49]. Further, in a study conducted in three cadaveric proximal femurs scanned at 7T (0.130 mm × 0.130 mm × 1.5 mm, acq. time 16 min) and using μCT, Soldati et al. reported no statistical difference between the methods and so for the whole set of morphological parameters [42]. These preliminary results strongly suggest that UHF MRI could be of interest for the in vivo assessment of bone microarchitecture particularly for the deep anatomical regions.

2.6. Comparison with CT Measurements

Validation of the bone morphological parameters derived from the high-resolution MR images has usually been performed through the comparison with X-ray based techniques (qCT, HRpQCT, and μCT).

2.6.1. Ex-vivo

Ex vivo studies have been performed in different body parts. However, due to the samples size (<5 cm^3) and the commonly used preparation protocols (replacement of marrow), they remain poorly representative of the in vivo conditions [13][39][42][67][81]. One of the first studies validating MR bone structure measurements was performed by Hipp et al. in cubic bovine trabecular bone from several anatomical sites using optical and micro-MRI methods. BVF and Tb.N were linearly related ($r^2 = 0.81$ and $r^2 = 0.53$ respectively) and did not differ statistically ($p = 0.96$ and $p = 0.17$) [39][81]. These results were confirmed and extended in human specimens by Majumdar et al., in a study conducted in 7 cubic specimens of trabecular bone extracted from cadaveric radii scanned at 1.5T (0.156 mm × 0.156 mm × 0.3 mm) and using μCT (0.018 mm isovolumetric). The results showed a good correlation for the whole set of metrics with BVF and Tb.Th performing the best (r = 0.77 and 0.87 respectively) and Tb.Sp and Tb.N the worst (r = 0.53 and 0.6 respectively). However a significative statistical difference ($p > 0.01$) was reported for all the calculated features [13]. MRI images with an in plane pixel-size lower than the smallest trabecular thickness order (0.1 mm) are not easily reachable. On that basis, one cannot expect to fully characterize it. Moreover, these findings were further extended in a larger study conducted in 39 distal radius specimens scanned at 1.5T MRI (0.152 mm × 0.152 mm × 0.9 mm) and using contact radiography (0.05 mm

71. Griffith, J.F.; Yeung, D.K.W.; Antonio, G.E.; Lee, F.K.H.; Hong, A.W.L.; Wong, S.Y.S.; Lau, E.M.C.; Leung, P.C. Vertebral Bone Mineral Density, Marrow Perfusion, and Fat Content in Healthy Men and Men with Osteoporosis: Dynamic Contrast-Enhanced MR Imaging and MR Spectroscopy. Radiology 2005, 236, 945–951, doi:10.1148/radiol.2363041425.
72. Woods, G.N.; Ewing, S.K.; Sigurdsson, S.; Kado, D.M.; Eiriksdottir, G.; Gudnason, V.; Hue, T.F.; Lang, T.F.; Vittinghoff, E.; Harris, T.B.; et al. Greater Bone Marrow Adiposity Predicts Bone Loss in Older Women. J. Bone Miner. Res. 2020, 35, 326–332, doi:10.1002/jbmr.3895.
73. Chang, G.; Rajapakse, C.S.; Chen, C.; Welbeck, A.; Egol, K.; Regatte, R.R.; Saha, P.K.; Honig, S. 3-T MR Imaging of Proximal Femur Microarchitecture in Subjects with and without Fragility Fracture and Nonosteoporotic Proximal Femur Bone Mineral Density. Radiology 2018, 287, 608–619, doi:10.1148/radiol.2017170138.
74. Kindler, J.M.; Pollock, N.K.; Ross, H.L.; Modlesky, C.M.; Singh, H.; Laing, E.M.; Lewis, R.D. Obese Versus Normal-Weight Late-Adolescent Females Have Inferior Trabecular Bone Microarchitecture: A Pilot Case-Control Study. Calcif Tissue Int 2017, 101, 479–488, doi:10.1007/s00223-017-0303-2.
75. Mulder, M.J.; Keuken, M.C.; Bazin, P.-L.; Alkemade, A.; Forstmann, B.U. Size and Shape Matter: The Impact of Voxel Geometry on the Identification of Small Nuclei. PLoS ONE 2019, 14, e0215382, doi:10.1371/journal.pone.0215382.
76. Koshi, R. Cunningham's Manual of Practical Anatomy VOL 1 Upper and Lower limbs, 16th ed.; OUP: Oxford, UK, 2017; Volume 1; ISBN 978-0-19-874936-3.
77. Van Oostwaard, M. Osteoporosis and the Nature of Fragility Fracture: An Overview. In Fragility Fracture Nursing; Hertz, K., Santy-Tomlinson, J., Eds.; Perspectives in Nursing Management and Care for Older Adults; Springer International Publishing: Cham, Switzerland, 2018; pp. 1–13; ISBN 978-3-319-76680-5.
78. Liu, C.; Liu, C.; Si, L.; Shen, H.; Wang, Q.; Yao, W. Relationship between Subchondral Bone Microstructure and Articular Cartilage in the Osteoarthritic Knee Using 3T MRI: Interrelationships in the OA Knee. J. Magn. Reson. Imaging 2018, 48, 669–679, doi:10.1002/jmri.25982.
79. Bolbos, R.I.; Zuo, J.; Banerjee, S.; Link, T.M.; Benjamin Ma, C.; Li, X.; Majumdar, S. Relationship between Trabecular Bone Structure and Articular Cartilage Morphology and Relaxation Times in Early OA of the Knee Joint Using Parallel MRI at 3T. Osteoarthr. Cartil. 2008, 16, 1150–1159, doi:10.1016/j.joca.2008.02.018.
80. Abdulaal, O.M. Evaluation of Optimised 3D Turbo Spin Echo and Gradient Echo MR Pulse Sequences of the Knee at 3T and 1.5T. 9. Radiography 2020, doi:10.1016/j.radi.2020.09.020.
81. Folkesson, J.; Goldenstein, J.; Carballido-Gamio, J.; Kazakia, G.; Burghardt, A.J.; Rodriguez, A.; Krug, R.; de Papp, A.E.; Link, T.M.; Majumdar, S. Longitudinal Evaluation of the Effects of Alendronate on MRI Bone Microarchitecture in Postmenopausal Osteopenic Women. Bone 2011, 48, 611–621, doi:10.1016/j.bone.2010.10.179.
82. Jarraya, M.; Heiss, R.; Duryea, J.; Nagel, A.M.; Lynch, J.A.; Guermazi, A.; Weber, M.-A.; Arkudas, A.; Horch, R.E.; Uder, M.; et al. Bone Structure Analysis of the Radius Using Ultrahigh Field (7T) MRI: Relevance of Technical Parameters and Comparison with 3T MRI and Radiography. Diagnostics 2021, 11, 110, doi:10.3390/diagnostics11010110.
83. Weiger, M.; Stampanoni, M.; Pruessmann, K.P. Direct Depiction of Bone Microstructure Using MRI with Zero Echo Time. Bone 2013, 54, 44–47, doi:10.1016/j.bone.2013.01.027.
84. Kazakia, G.J.; Hyun, B.; Burghardt, A.J.; Krug, R.; Newitt, D.C.; de Papp, A.E.; Link, T.M.; Majumdar, S. In Vivo Determination of Bone Structure in Postmenopausal Women: A Comparison of HR-PQCT and High-Field MR Imaging. J. Bone Miner. Res. 2007, 23, 463–474, doi:10.1359/jbmr.071116.
85. Wu, H.-Z.; Zhang, X.-F.; Han, S.-M.; Cao, L.; Wen, J.-X.; Wu, W.-J.; Gao, B.-L. Correlation of Bone Mineral Density with MRI T2* Values in Quantitative Analysis of Lumbar Osteoporosis. Arch. Osteoporos 2020, 15, 18, doi:10.1007/s11657-020-0682-2.
86. Bandirali, M.; Leo, G.D.; Papini, G.D.E.; Messina, C.; Sconfienza, L.M.; Ulivieri, F.M.; Sardanelli, F. A New Diagnostic Score to Detect Osteoporosis in Patients Undergoing Lumbar Spine MRI. Eur. Radiol. 2015, 25, 2951–2959 .
87. Adams, J.E. Quantitative Computed Tomography. Eur. J. Radiol. 2009, 71, 415–424, doi:10.1016/j.ejrad.2009.04.074.
88. Fazeli, P.K.; Horowitz, M.C.; MacDougald, O.A.; Scheller, E.L.; Rodeheffer, M.S.; Rosen, C.J.; Klibanski, A. Marrow Fat and Bone—New Perspectives. J. Clin. Endocrinol. Metab. 2013, 98, 935–945 .
89. Van Oostwaard, M. Osteoporosis and the Nature of Fragility Fracture: An Overview. In Fragility Fracture Nursing; Hertz, K.,Santy-Tomlinson, J., Eds.; Perspectives in Nursing Management and Care for Older Adults; Springer International Publishing:Cham, Switzerland, 2018; pp. 1–13; ISBN 978-3-319-76680-5.

0.61) between bone microstructure parameters derived from both methods with Tb.Sp and BVF providing the highest correlations (r = 0.69 and p = 0.75 respectively) [67]. More recently, Rajakapse et al. conducted a study in 13 cylindrical specimens (7 proximal femurs, 3 proximal tibiae, and 3 third lumbar vertebrae) extracted from 7 human donors and computed microarchitectural parameters using 9.4T micro-MRI (0.050 mm isovolumetric) and µCT (0.021 mm isovolumetric). Architectural parameters were found to highly correlate between these two modalities with a slope close to unity (r^2 ranging from 0.78 to 0.97) [82]. In a more recent study conducted in three cadaveric entire proximal femurs evaluating the trabecular morphology using 7T MRI (0.13 mm × 0.13 mm × 1.5 mm) and comparing the results with those acquired using µCT (0.051 mm isovolumetric) (Figure 1), Soldati et al. showed a good intraclass correlation coefficient for all the parameters (ICC > 0.54) between 7T and µCT [42] illustrating that bone morphological metrics of human specimens can be properly assessed using MRI. Moreover, due to the comparison between MR images and gold standard high-resolution CT images, it has been shown that trabecular features derived from images with a similar pixel size provide statistically comparable results. However, when assessing bone trabeculae using MRI, partial volume effects will occur and will affect image segmentation and trabeculae quantification.

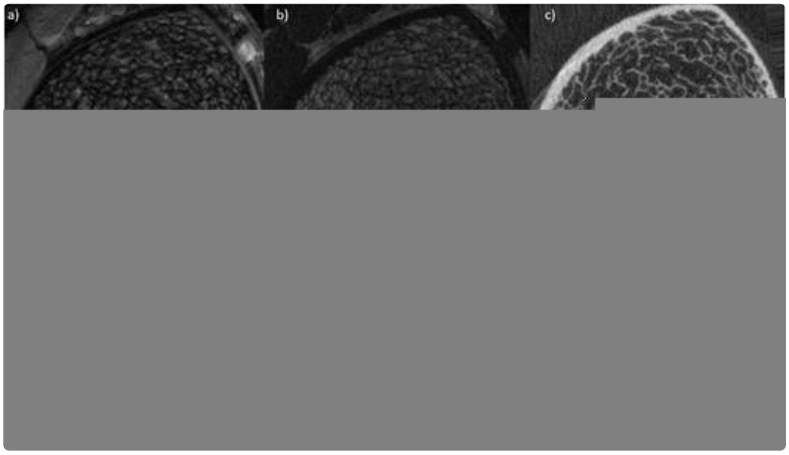

Figure 1. Comparison between MRI and CT. (first row) MR images of in vivo distal tibia acquired using gradient echo sequence at 7T MRI (**a**) (0.156 mm × 0.156 mm × 0.5 mm) and 3T MRI (**b**) (0.156 mm × 0.156 mm × 0.5 mm), and compared with high-resolution peripheral computed tomography (HR-pQCT) (**c**) (0.082 mm^3) (reproduced from J. of Mag. Res. Im. 27:854–859 (2008)). (second row) MR images of cadaveric proximal femur acquired using turbo spin echo sequence at 7T MRI (**d**) (0.13 mm × 0.13 mm × 1.5 mm) and 3T MRI (**e**) (0.21 mm × 0.21 mm × 1.1 mm), and compared with µCT (**f**) (0.051 mm^3). Note that using MRI, the trabecular bone appears black and bone marrow delivers the bright signal whereas for HR-pQCT and µCT the trabecular bone is shown bright. Additionally, note that the trabecular network is clearly more enhanced at 7T compared to 3T.

2.6.2. In-Vivo

The MRI potential for the bone microstructure has also been assessed in vivo in anatomical regions more affected by osteoporosis, i.e., tibiae and radii, vertebrae [24][83][84], distal [18][73][74][75][85], and proximal femurs [30][32][31]. Microarchitectural parameters extrapolated from 3T MRI (0.156 mm × 0.156 mm × 0.5 mm) and compared to HR-pQCT of tibiae and radii of 11 healthy volunteers showed good correlation for BVF (r = 0.83) and Tb.Sp (r = 0.7) in tibiae and good correlation for all the microarchitecture parameters investigated in radii (r = 0.65, 0.95, 0.83, and 0.63 for BVF, Tb.N, Tb.Sp, and Tb.Th respectively) [38]. Kazakia et al. extended these results in a study conducted in tibiae and radii of 52 postmenopausal scanned at 3T MRI (0.156 mm × 0.156 mm × 0.5 mm) and using HR-pQCT. A significant correlation between MRI and HR-pQCT has been reported for Tb.N (r^2 = 0.52) and Tb.Sp (r^2 = 0.54–0.60) with no statistical difference for these two parameters. Poor correlations were reported for BVF and Tb.Th (r^2 = 0.18–0.34) [86]. Similar results were also reported by Folkesson et al., in a study conducted in 52 postmenopausal women scanned at 3T (0.156 mm × 0.156 mm × 0.5 mm) and using HR-pQCT in both tibiae and radii. All the structural parameters derived from MRI were highly correlated to those obtained from HR-pQCT (Tb.N was equal to 0.68 and 0.73 and Tb.Sp was equal to 0.77 and 0.67 for tibiae and radii respectively) with the exception of BVF and Tb.Th for which correlations were less significant (BVF was equal to 0.61 and 0.39 and Tb.Th was equal to 0.43 and 0.32 for tibiae and radii respectively) [79]. Furthermore, Krug et al. confirmed and extended these results in a study conducted in distal tibiae of 10 healthy volunteers scanned at 3T and 7T (0.156 mm × 0.156 mm × 0.5 mm for both techniques). The results showed that microarchitectural parameters extracted from HR-pQCT images had higher correlation with those extracted from 7T MR images (r equal to 0.73 for BVF, 0.69 for Tb.N, 0.89 for Tb.Sp, and 0.13 for Tb.Th) as compared to 3T MR images (r = 0.83, 0.49, 0.67, and 0.15 for BVF, Tb.N, Tb.Sp, and Tb.N respectively) (Figure 1). Interestingly, the corresponding absolute values did only differ by 0.6% for 7T and 3% for 3T [49]. All the findings reported above indicate good correlations for Tb.Sp and Tb.N between MRI and HR-pQCT. In contrast, this was not the case for BVF and Tb.Th. The limited resolution in MRI leads to partial volume effects

responsible for the exclusion of the smallest trabeculae, while susceptibility artifacts enhance the remaining trabeculae leading to an overestimation of Tb.Th. This double effect seems limited when using UHF MRI. Indeed, good correlations were found between MRI and HR-pQCT metrics although a poor correlation was still existing for Tb.Th.